Electrochimica Acta 252 (2017) 200–207

Contents lists available at ScienceDirect

Electrochimica Acta

journal homepage: www.elsevier.com/locate/electacta

Combination of Nitrogen-Doped Graphene with MoS_2 Nanoclusters for Improved Li-S Battery Cathode: Synthetic Effect between 2D Components

Zhongtao Li, Shenzhen Deng, Rongfei Xu, Liangqin Wei, Xin Su, Mingbo Wu*

State Key Laboratory of Heavy Oil Processing, College of Chemical Engineering, China University of Petroleum(East China), Qingdao 266580, China

ARTICLE INFO

Article history:
Received 4 July 2017
Received in revised form 30 August 2017
Accepted 1 September 2017
Available online xxx

Keywords:
MoS_2
Nitrogen-doped
Graphene oxide
Li-S battery

ABSTRACT

Herein, a layer in layer nanocomposition of flower-shaped MoS_2 nanoclusters with nitrogen-doped reduced graphene oxide(N-RGO@MoS_2) has been successfully prepared by a facile hydrothermal method to build up 3D matrix for supporting sulfur. This approach will integrate the advantages and avoid the disadvantages of graphene and MoS_2 through synergetic effect to produce an outstanding Li-S battery cathode, such as high electronic conductivity of N-RGO to reach great rate performance; stronger interaction between MoS_2 and polysulfide to suppress the shuttle effect for an improved durability; the great compatibility between two 2D components avoids their self-aggregation to increase capacity through wrap around and adhesion effect with loaded sulfur. A series of samples with various content of MoS_2 are investigated to optimize the electrode performance. Finally, N-RGO@MoS_2-10/S delivers an optimal discharge capacity of 729.1 mAh g^{-1} at 0.3C with the coulombic efficiency of 97.3% after 180 cycles.

1. Introduction

Lithium-ion batteries (LIBs) are one of the most important power sources in portable electronic devices and electric vehicles due to the high electromotive force, long cycling durability and high energy density [1–4]. Despite this, their wider application is restricted due to the limited energy density of available cathode materials in some special fields. New cathode materials need to be developed for meeting the request of higher energy density power source, among which sulfur is considered to be one of the most promising cathode for next-generation LIBs due to the high theoretical capacity (1672 mAh g^{-1}) [5], abundant reserves and nontoxic nature. However, the main drawbacks hindering Li-S battery practical application are followed: 1. poor conductivity of sulfur deteriorates batteries' rate performance; 2. volumetric change and polysulfide (Li_2S_n, 4< n <8) shuttling during cycling lead to the capacity degradation.

So far, a number of strategies have been tested to overcome the obstacles of sulfur cathode. One major improvement is made by employing conducting carbons to encapsulate sulfur to improve the conductivity of sulfur cathode and prevent the polysulfide shuttling simultaneously, such as porous carbon [6,7], graphene nanosheets [8–11], conducting polymers [12,13], hollow carbons [14,15] and carbon nanotubes [16,17]. Among these candidates, 2D graphene possesses outstanding performance due to high electrical conductivity and large surface area, which may help it to wrap around sulfur particles to build a conducting network resulting in larger capacity and better rate performance. Additionally, the volume change and polysulfide shuttling can be alleviated during cycling by the flexibility of conjugated graphene sheets, which leads to improved cycling performance. However, earlier study confirmed that these nonpolar carbon-based materials possess weak interaction with polar Li_2S_n species, which can still lead to graduate capacity fading upon long-term cycle [18].

Recent studies have also given rising focus on metal oxides to bind polysulfide, such as Al_2O_3 [19], SiO_2 [20], TiO_2 [21] and MnO_2 [22], which typically contains strong polarized surface that composed by metal-oxygen bond to afford abundant polar active sites for absorption of polysulfide. The addition of oxide nanostructures as functional absorbents can effectively suppress the shuttle effect of Li-S batteries. Compared to nonconductive metal oxide, some metal sulfides have better conductivity attributed to

* Corresponding author.
E-mail address: wumb@upc.edu.cn (M. Wu).

http://dx.doi.org/10.1016/j.electacta.2017.09.001
0013-4686/

the denser electron atmosphere and unique band structures. Additionally, metal-sulfur bonds can better bind polysulfide through stronger S···S interaction and dipolar interaction of metal-sulfur bonds on polarized surface.

2D layered metal sulfides with analogous structures to graphite, such as MoS_2 [23], WS_2 [24] and SnS_2 [25] have been proved an outstanding performance as LIBs electrode. As candidate materials of Li-S cathode, the open framework of these types of materials offers large surface area and allows a better connection with sulfur particles through wrap around and adhesion effect. Especially, MoS_2 have been proven to be highly efficient in depressing polysulfides shuttle to a longer cycle stability. Cui et al. [26,27] confirms that there are strong binding energies between Li_2S and the edge sites of MoS_2. Xing et al. [28] synthesizes hierarchical MoS_2/SnO_2 nanocomposites and confirms that MoS_2 can increase the conductance of the composites.

Therefore, the low cost, readily available 2D metal sulfide-MoS_2 has been combined with reduced graphene oxide (RGO) by a facile hydrothermal method to build up conductive matrix for Li-S battery in here. This approach would integrate the advantages and avoid the disadvantages of graphene and MoS_2 through synergetic effect to produce an outstanding Li-S battery, such as high electronic conductivity of RGO to reach great rate performance; MoS_2 as functional absorbents to suppress the shuttle effect of polysulfide to improve battery's durability; the layer in layer structure of two 2D components avoids their self-aggregation to increase capacity of cathode through enlarged surface area for sulfur loading.

2. Experimental

2.1. Preparation of N-RGO/S

Graphite oxide was first prepared from graphite powder via a modified Hummers' method [29] reported elsewhere. Afterwards, graphite oxide was exfoliated in water with ultrasonic treatment for 4 h to form a colloidal suspension (100 mL, 2 mg mL^{-1}). Then, sulfourea was dissolved into the suspension and then transferred and sealed into Teflon-lined stainless steel autoclave, which was heated at 200 °C for 20 h in a constant temperature oven. After cooling down to ambient temperature naturally, the samples were finally dried in the freeze dryer.

The N-RGO/S composites were prepared through a melt-diffusion technique. Typically, the sublimed sulfur and N-RGO at mass ratio of 65:35 were added to the CS_2 to form a uniform dispersion solution, then dried under magnetic stirring at 45 °C. Afterwards, the dried sample put into a sealed vacuum glass tube, then the glass tube put into quartz tube furnace in N_2 atmosphere and kept the temperature at 155 °C for 12 h. The final N-RGO/S was obtained by further treatment at 200 °C for 2 h under N_2 condition to remove redundant sulfur from the surface of the composites.

2.2. Preparation of N-RGO@MoS_2-n/S

200 mg graphite oxide was exfoliated in a mixture of 50 mL deionized (DI) water and 50 mL ethylene glycol with ultrasonic treatment for 4 h to form a colloidal suspension. 33.6 mg $Na_2MoO_4{\cdot}2H_2O$, 80 mg $(NH_2)_2CS$, and 15 mg polyethylene glycol (PEG-20000) were successively dissolved into another 30 mL DI water and then stirred for 0.5 h. Afterwards, the two solutions were mixed together under vigorous stirring. Subsequently, this mixed solution was transferred and sealed into Teflon-lined stainless steel autoclave, which was heated at 200 °C for 20 h in a constant temperature oven and then cooled down to ambient temperature naturally. Finally, the precipitate powder was centrifuged and washed several times with ethanol and DI water, and dried in the freeze dryer.

By adjusting amount of $Na_2Mo_2O_4{\cdot}2H_2O$, we synthesized N-RGO@MoS_2 composites as controling samples with various MoS_2 mass contents of 25%, 10% and 5%, which were labelled as N-RGO@MoS_2-25, N-RGO@MoS_2-10, N-RGO@MoS_2-5, respectively.

The N-RGO@MoS_2/S composites were prepared through a melt-diffusion technique as mentioned above. The sulfur filled composites with different MoS_2 contents were labelled as N-RGO@MoS_2-25/S, N-RGO@MoS_2-10/S, N-RGO@MoS_2-5/S, respectively.

2.3. Adsorption capability

0.05 M polysulfide solution was prepared with mixing Li_2S_6 and DME/DOL. The samples were dried for 12 h under vacuum; 25 mg sample was placed into 5 mL of the lithium polysulfide solution in an argon-filled glove box for 24 h to adsorption equilibration.

2.4. Samples characterization

The structures and morphologies of obtained composites were characterized with X-ray diffraction (XRD, X'Pert PRO MPD, Holland), field emission scanning electron microscopy (FE-SEM) (Hitachi S-4800, Japan), and transmission electron microscopy (TEM, JEM-2100UHR, Japan). Nitrogen sorption isotherms were measured at 77 K with an ASAP 2020 analyzer (Micromeritics, US). The Brunauer–Emmett–Teller (BET) surface area was calculated from the adsorption data. The pore size distribution was calculated by the density functional theory (DFT) method from the adsorption branches of the isotherms. The functional groups in the samples were studied by X-ray photoelectron spectroscopy (XPS, Thermo Scientific ESCALab250Xi). The weight ratio of sulfur in the composite was determined by thermogravimetric analysis (TGA, STA 409 PC Luxx, Germany).

2.5. Electrochemical measurements

The electrochemical measurements were conducted using CR2032 coin cells with pure Li foil as the counter and reference electrode at room temperature. Working electrodes consist of obtained samples, carbon black and polyvinylidene difluoride in a weight ratio of 7:2:1 in N-methyl-2-pyrrolidinone. The slurry was coated onto a current collector made from aluminium foil and then was dried under vacuum at 60 °C for 12 h. The electrodes were cut to disks typically with a diameter of 12 mm, and the average mass of the sulfur loading within the coin cells is around 1.5-2.0 mg cm^{-2}. The cells assembly were carried out in an Ar-filled glovebox with the concentration of moisture and oxygen below 0.1 ppm. The separator was microporous polypropylene and the organic electrolyte was composed of 1.0 M LiTFSI in 1,2-dimethoxyethane and 1,3-dioxolane (DME/DOL, 1:1 vol) with 1.0% $LiNO_3$ (analytical grade). The galvanostatic discharge-charge cycle tests and rate tests were carried out on a Land Battery Measurement System (Land CT2001A, China) at various current densities of 0.3-4C (1C = 1672 mA g^{-1}) with a cutoff voltage of 1.5-3.0 V vs. Li/Li^+ at room temperature. The specific capacity was calculated based on the mass of sulfur. Cyclic voltammetry (CV) curves were conducted using an Ametek PARSTAT4000 electrochemistry workstation between 1.5 and 3.0 V at a scan rate of 0.1 mV s^{-1}. Electrochemical impedance spectroscopy (EIS) tests were also performed using Ametek PARSTAT4000 electrochemistry workstation in the frequency range of 100 kHz to 10 mHz with AC voltage amplitude of 10 mV.

3. Results and discussion

The synthetic strategy of N-RGO@MoS_2/S nanohybrids are illustrated in Scheme 1. In the first, the nitrogen source (sulfourea) and various amount of $Na_2MoO_4{\cdot}2H_2O$ are mixed with GO through solvothermal process for preparing nitrogen-doped reduced graphene oxide with MoS_2 nanosheets(N-RGO@MoS_2). The functional groups on the surface of GO, such as carboxyl, hydroxyl and epoxy groups, contribute to improved coordination on the surface with Mo ions to form well-distributed MoS_2 after reduction of $(NH_2)_2CS$. The 2D MoS_2 nanosheets are warped together to form nanoclusters on the surface of RGO, which can block self-aggregation of RGO nanosheets. Then, the fully freeze dried combinations N-RGO@MoS_2 are used for preparing Li-S cathode RGO@MoS_2-n/S by diffusion of melted sulfur into the conductive matrix. To better understanding the synergetic effect of each components, various samples with different content of MoS_2 have been synthesized, namely N-RGO@MoS_2-5, N-RGO@MoS_2-10, N-RGO@MoS_2-25.

The crystal structures of sample N-RGO@MoS_2-10 are characterized by X-ray powder diffraction (XRD), as shown in Fig. 1a. The weak diffraction peaks at 14.3°, 33.5° and 58.3° in the curve of N-RGO@MoS_2-10 (blue line) can be assigned to (002), (101) and (110) planes of hexagonal MoS_2 (JCPDS, No. 37-1492), implying the formation of crystalline MoS_2. N-RGO displays two diffraction peaks at 26.1° and 42.7°, which can be ascribed to the (002) and (100) reflection planes of conjugated layers, respectively (JCPDS 26-1077) [30]. Furthermore, the diffraction peaks of N-RGO in N-RGO@MoS_2-10 are left shifted to 24.1°, which indicates an increasing of the space between N-RGO layers with the introduction of MoS_2 [31,32]. In addition, the diffraction peaks of MoS_2 in N-RGO@MoS_2-10 are low and broad, which indicates the formation of MoS_2 nanolayer and well-dispersion on the surface of N-RGO layers.

The porous structure of the N-RGO and N-RGO@MoS_2-10 is characterized by nitrogen adsorption/desorption isotherms. Fig. 1b shows a joint curve of type I and type IV, suggesting a micro-mesoporous hybrid structure. The calculated BET equivalent surface area and the adsorption total pore volume of N-RGO@MoS_2-10 are 223.1 $m^2 g^{-1}$ and 0.25 $cm^3 g^{-1}$, respectively, which is much higher than those of N-RGO (131.1 $m^2 g^{-1}$ and 0.15 $cm^3 g^{-1}$). Combined with the result of SEM images (Fig. 1d and e), the introduction of MoS_2 seems to effectively avoid the self-aggregation RGO, which increases the surface areas and pore volume of the nanocomposites. The pore size distribution plot obtained by the DFT method (Fig. 1c) shows that the N-RGO@MoS_2-10 possesses a hierarchical porosity structure that consists with micropores and mesopores. As previous research, the hierarchical porous structure is beneficial for maximizing the sulphur-loading and enhancing the electrolyte penetration [33,34].

To accurately calculate the content of sulfur in samples N-RGO@MoS_2/S, the TGA date from rt. to 700 °C is tested in N_2 atmosphere with scan rate at 10 °C·min^{-1}. As shown in Fig. S1, the major mass loss occurs in the range of 220–350 °C, and the mass contents of sulfur in the N-RGO@MoS_2-25/S, N-RGO@MoS_2-10/S, N-RGO@MoS_2-5/S and N-RGO/S are around 63.5%, 65.0%, 64.8% and 64.5%, respectively. The starting point and end point of mass loss are both higher than that of pure sulfur (180–280 °C) [35], which may be due to the enhanced interaction between nanohybrids and sulfur.

Fig. S2 shows a typical SEM image of MoS_2, which is dominated by flower-shaped nanoclusters with rough surface. The average diameter of these particles is about 800 nm, which are composed of warped MoS_2 sheets. SEM and TEM images of N-RGO@MoS_2-n and N-RGO@MoS_2-10/S are exhibited in Figs. 2 and Fig. S3. In Fig. 2a, the flower-shaped MoS_2 nanoclusters are aggregated on N-RGO plane in sample N-RGO@MoS_2-25, but the average size of these particles decreased to 600 nm, which reveals the interaction between MoS_2 and N-RGO can weaken MoS_2 self-aggregation[33]. The shrank nanoclusters of MoS_2 can also be identified in TEM image (Fig. 2e) and SEM image (Fig. 2b) of N-RGO@MoS_2-10, but the density of nanoclusters on RGO surface is decreased. In Fig. 2d and Fig. S3b, isolated MoS_2 particles can't be found out in N-RGO@MoS_2-5, which indicates that MoS_2 nanoflakes are well-dispersed and adhered on the N-RGO surface due to the strong interaction between RGO and MoS_2. Fig. 2c shows the SEM image of N-RGO@MoS_2-10/S. After adding sublimed sulfur, the average diameter of MoS_2 nanospheres increases from 0.6 μm to 1.1 μm, which demonstrates that sulfur is absorbed into MoS_2 nanoclusters through strong interaction to improve sulfur utilization efficiency. In the TEM image of N-RGO@MoS_2-10/S (Fig. 2f), the lower contrast of nanospheres reveals the successful filling of sulfur into MoS_2 nanoclusters, and some 2D nanosheets structures can be identified inside the nanospheres.

Fig. 3 shows the TEM images and elemental mapping of N-RGO@MoS_2-10. The high resolution image in Fig. 3b demonstrats the lamellar structure and exhibited lattice distance of 0.62 nm corresponding to the (002) plane of MoS_2. As a corresponding of XRD data (Fig. 1), the RGO lattice can be identified as 0.38 nm in Fig. 3c, which is slightly larger than that of traditional value (0.34 nm). The elemental mapping of N-RGO@MoS_2-10 in Fig. 3d demonstrats that carbon, nitrogen, sulfur and molybdenum are distributed uniformly in N-RGO@MoS_2-10. Fig. S4 shows the EDX pattern and relative element content of N-RGO@MoS_2-10, which approves the successful introduction of MoS_2 and N on GO matrix.

The chemical bonding states in as-prepared samples are analysed by X-ray Photoelectron Spectroscopy (XPS) spectra, and XPS full spectra of N-RGO@MoS_2-10 is shown in Fig. S5a. Fig. 4a and b shows the high resolution spectrum of S 2p peak of N-RGO@MoS_2-10 and N-RGO@MoS_2-10/S composite, respectively. Three sulfur environments of N-RGO@MoS_2-10 can identified into four components (Fig. 4a) at binding energies of 161.5 eV, 163.4 eV and 168.6 eV, respectively, which are corresponding to S^{2-}, S_2^{2-}, SO_4^{2-}/SO_3^{2-} and SO_4^{2-}/SO_3^{2-}. The appearance of SO_4^{2-}/SO_3^{2-} and SO_4^{2-}/SO_3^{2-} is produced by the oxidation of sulfur during the hydrothermal reaction [36]. After introduction of sulfur in N-RGO@MoS_2-10/S, a similar four components (S^{2-}, S_2^{2-}, S_8 and SO_4^{2-}/SO_3^{2-}) of sulfur environments can be identified, which are located at 162.1 eV, 163.6 eV, 164.8 eV and 168.8 eV (Fig. 4b), respectively. It is worth mentioning that both binding energies of

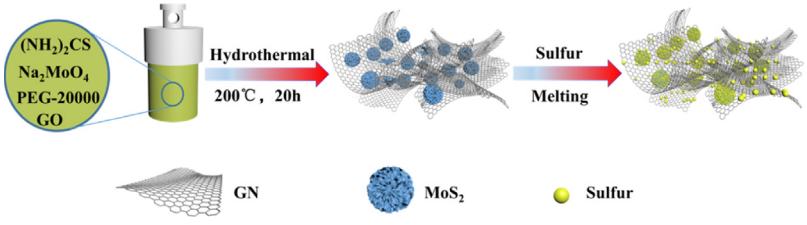

Scheme 1. Schematic of synthesis process for N-RGO@MoS_2/S.

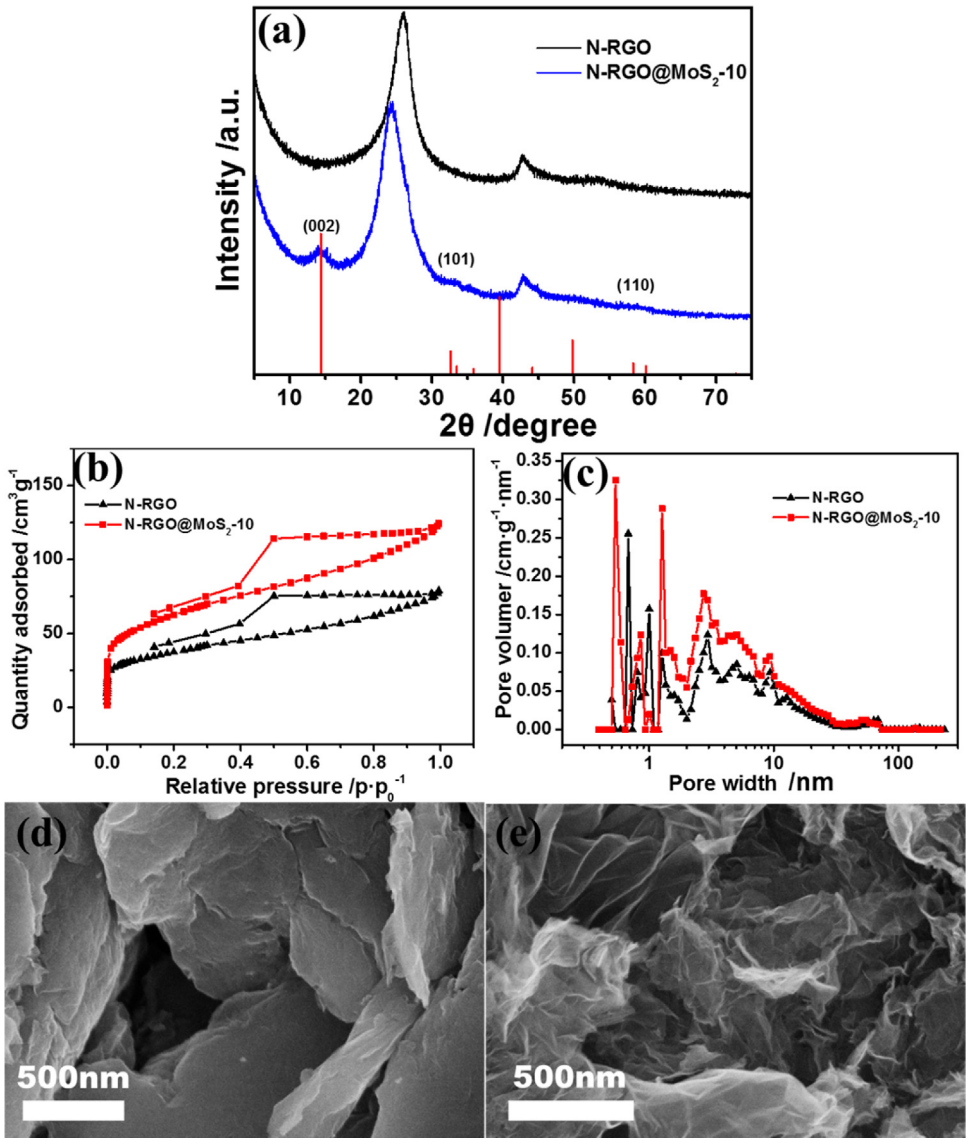

Fig. 1. (a) XRD patterns, (b) Nitrogen adsorption/desorption isotherms and (c) the corresponding pore-size distribution curves of the synthesized N-RGO and N-RGO@MoS_2-10 samples, (d) SEM images of N-RGO, (e) SEM images of N-RGO@MoS_2-10.

S^{2-} and S_2^{2-} are higher than those in N-RGO@MoS_2-10 (161.5 and 163.4 eV), which implies that the electron deficient S atoms in element sulfur accept electrons from S^{2-} and S_2^{2-} in MoS_2 and lead to an increasing of the interaction between element sulfur and MoS_2. Fig. 4c-d shows the high resolution spectrum of Mo^{3d}-S^{2s} peak in N-RGO@MoS_2-10 and N-RGO@MoS_2-10/S, respectively. The peak located at 226.1 eV of N-RGO@MoS_2-10 spectra corresponds to the S 2s of divalent sulfide ions (S^{2-}). The two main peaks at 228.8 eV (Mo 3d3/2) and 232.3 eV (Mo 3d5/2) can be assigned to the Mo(IV), while the peak at 235.4 eV corresponds to Mo(VI) due to partial oxidation of Mo(IV) [37]. In the data of N-RGO@MoS_2-10/S, a new peak appears at 227.9 eV, which could be assigned to S 2s of element sulfur.

Fig. S5b and c exhibit the high resolution spectrums of C 1s peak for GO and N-RGO@MoS_2-10. The high resolution C 1s spectrum of GO (Fig. S5b) reveals a considerable oxidation degree with four resolved peaks at 284.8 eV, 286.6 eV, 287.3 eV, and 288.2 eV, respectively, corresponding to sp2-hybridized C-C/C=C and oxygenated functional groups (C-O, C=O and O—C=O) [38]. While in the C 1s fitting spectrum of N-RGO@MoS_2-10 (Fig. S5c), only C-C/C=C, O-C peaks are present, which suggests that most oxygen-containing functional group are reduced after N doping. Besides, a new peak appears at 285.5 eV in N-RGO@MoS_2-10, which further confirms the formation of C-N bond [36,39] during hydrothermal process. N 1s 3p XPS spectra of N-RGO@MoS_2-10 is showed in Fig. S5d. The sample mainly contains pyridnic N (398.3 eV), pyrrolic N (399.7 eV) and quaternary N (400.9 eV), which are supposed to improve the electrical conductivity and accelerate the charge transfer during cycling as well as enhance the binding between composite and polysulfides [40].

Fig. 5a shows the cyclic voltammetry profiles of the N-RGO@MoS_2-10/S electrode for the 1st, 2nd, and 3th cycles at a sweep rate of 0.1 $mV \cdot s^{-1}$ in the potential range of 1.5-3.0 V (vs Li/Li^+). The curves exhibit two main reduction peaks at about 2.28 and 1.98 V, which attributes to the two-step reduction reaction of sulfur in the discharge process. One oxidation peak is observed in the charge process at about 2.48 V. These peaks are well fitted to two discharge plateaus and one charge plateau in galvanostatic charge/discharge profile of Fig. 5b. According to the electrochemical reaction mechanism of sulfur, the peak at high voltage of 2.28 V (vs Li/Li^+) corresponds to elemental sulfur transforming to the soluble polysulfides (Li_2S_x, $4 \leq x \leq 8$) during the discharge process,

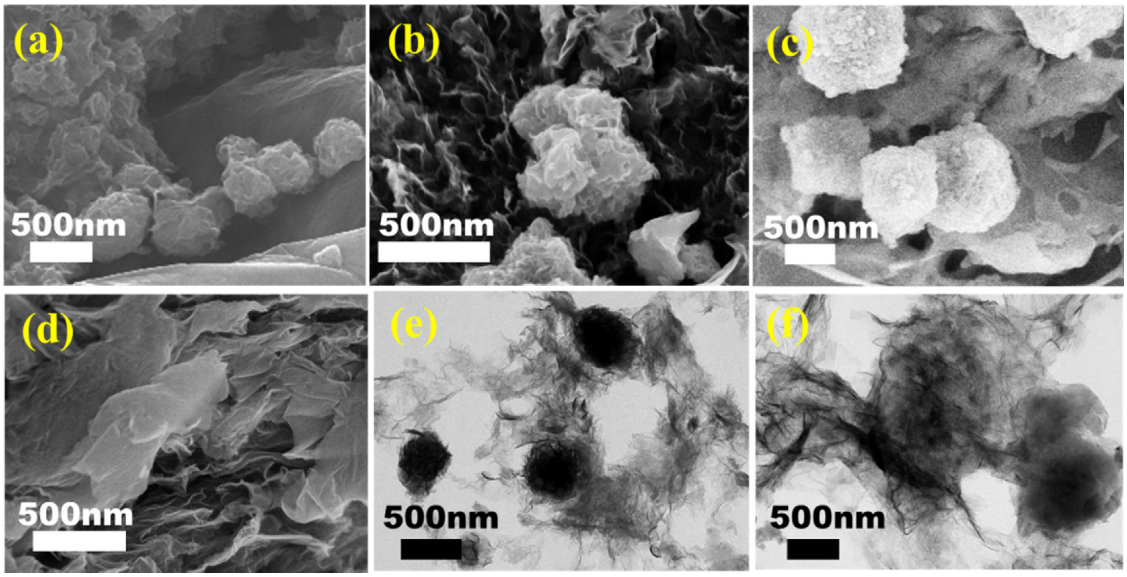

Fig. 2. SEM and TEM images of materials for (a, e) N-RGO@MoS_2-25, (b, f) N-RGO@MoS_2-10, (c, g) N-RGO@MoS_2-5 and (d, h) N-RGO@MoS_2-10/S.

and the low-voltage peak corresponds to the soluble polysulfides producing insoluble polysulfides Li_2S_2 and Li_2S. Likewise, one conspicuous oxidation peak at around 2.48 V relates to the transformation of Li_2S_2/Li_2S to S_8 [41]. From the second cycle onward, the reduction peak at 1.98 V and the oxidation peak at 2.48 V are slightly shifted to lower potential (1.97 V for cathodic peak and 2.43 V for anodic peak). The slight narrower voltage gap between oxidation and reduction peaks can reduce the electrode polarization and improve the charge transfer kinetics, which means the reduction and oxidation becomes more easies in the subsequent cycles after the activation in the first cycle [42]. The almost overlapped CV curves of the second and third cycles indicated highly reversible redox behaviour and good cycling stability of N-RGO@MoS_2-10/S nanohybrids, and similar results can also be observed in the voltage-capacity profiles Fig. 5b. In addition, the reduction peak at about 1.7 V in the first cycle attributes to the formation of SEI (solid electrolyte interface), which disappeared in the following cycles.

The cycle performance of cell for N-RGO/S and N-RGO@MoS_2-10/S electrodes at a current density of 0.3C in the voltage range of 1.5-3.0 V is shown in Fig. 5c. As revealed in Fig. 5c, the N-RGO@MoS_2-10/S electrode delivers the specific capacity of 729.1 mAh g^{-1}, and the coulombic efficiency keeps over 97.3% after 180 cycles. In contrast, the N-RGO/S only delivers the specific capacity of 482.4 mAh g^{-1}, and the coulombic efficiency is 83.9% after 180 cycles. The MoS_2/S delivers the specific capacity of 503.7 mAh g^{-1} after 180 cycles (Fig. S6). N-RGO@MoS_2-10/S electrode exhibits higher cycling specific capacity and coulombic efficiency than the N-RGO/S and MoS_2/S electrodes, which indicates that the introduction of MoS_2 into N-RGO matrix can increase conductivity, inhibit shuttle effect and enhance the coulombic efficiency. The long-time cycle performance of cell N-RGO@MoS_2-10/S electrode at a current density of 0.5C in the voltage range of 1.5-3.0 V is shown in Fig. S7. The N-RGO@MoS_2-10/S electrode delivers the specific capacity of 449.7 mAh g^{-1}, and the coulombic efficiency keeps 96.4% even after 600 cycles.

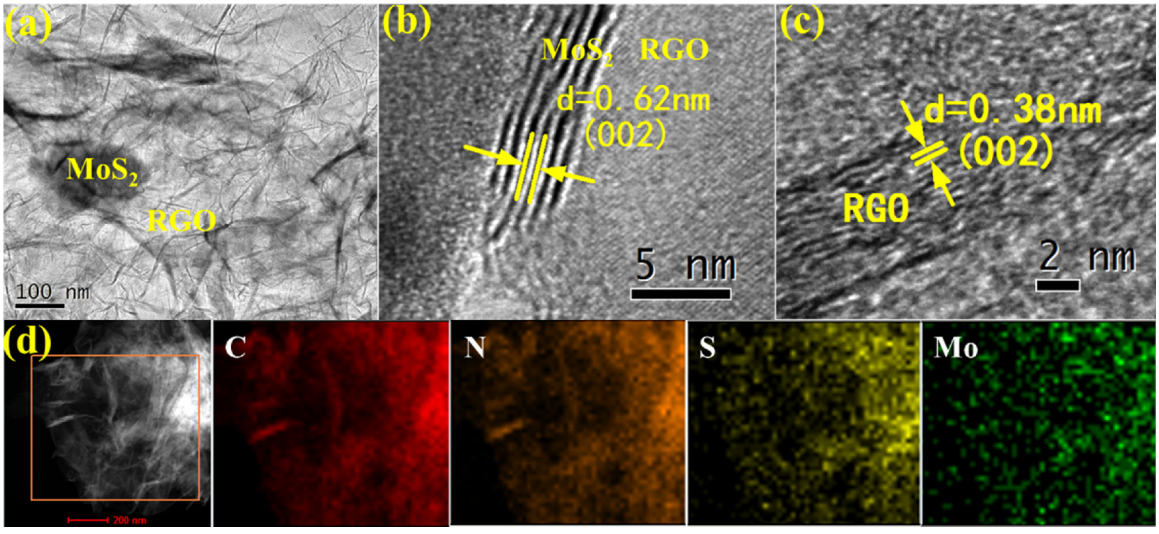

Fig. 3. (a) TEM images of N-RGO@MoS_2-10, (b-c) HRTEM images of N-RGO@MoS_2-10, (d) TEM bright field (BF) image and the corresponding elemental mapping for C, N, S, Mo of N-RGO@MoS_2-10.

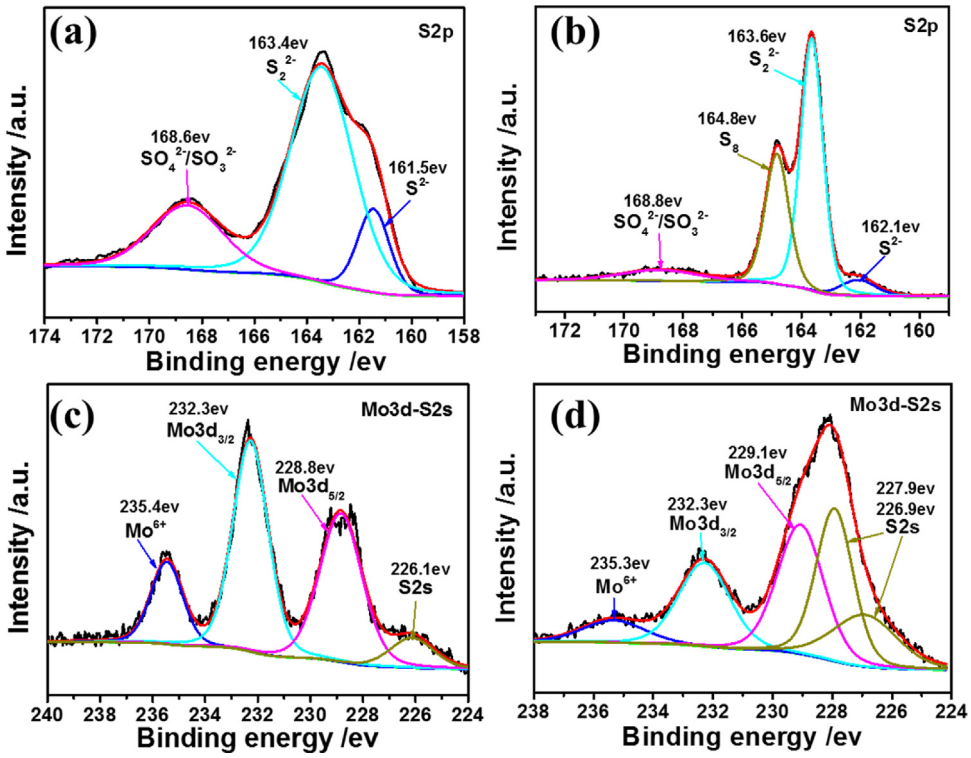

Fig. 4. S2p XPS spectrum of (a) N-RGO@MoS_2-10 and (b) N-RGO@MoS_2-10/S; Mo3d-S2s XPS spectrum of (c) N-RGO@MoS_2-10 and (d) N-RGO@MoS_2-10/S.

In order to further study the effect of MoS_2 in composites, the cyclic performance of composites with different MoS_2 contents were tested. As revealed in Fig. 5c, the reversible discharge capacity and coulombic efficiency of N-RGO@MoS_2-25/S and N-RGO@MoS_2-5/S keep 590.1 mAh g^{-1} and 98.3%, 554.1 mAh g^{-1} and 87.6% respectively after 180 cycles, both of which are lower than that of N-RGO@MoS_2-10/S. The remarkable improved stability of N-RGO@MoS_2-10/S can be attributed to optimized balance between polar MoS_2 and conductive RGO. The introduction of moderate amount MoS_2 and nitrogen atoms to reduce GO can not only increase binding energy between S and substrate to reach a high stable nanostructure, but also play as conductive matrix to support smaller and well-dispersed MoS_2 nanoparticles for facile Li^+ penetration and charges transfer. The worse performance of N-RGO@MoS_2-25/S can be due to the higher content of MoS_2, which renders the inorganic nanoparticles congregate together and

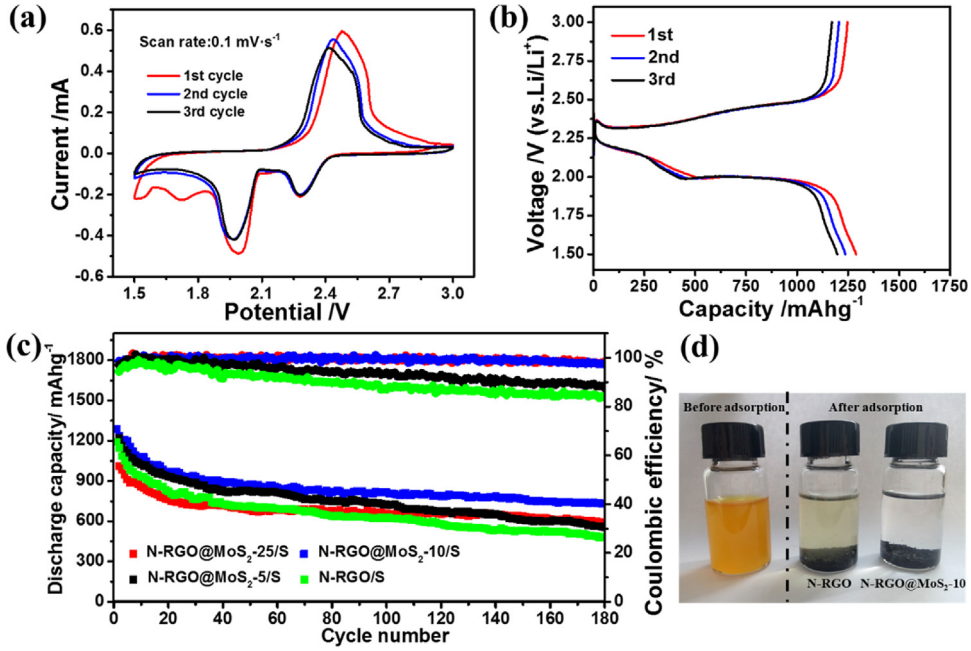

Fig. 5. (a) Cyclic voltammetry curves of N-RGO@MoS_2-10/S electrodes at a sweep rate of 0.1 mV s^{-1} in the potential range 1.5-3.0 V, (b) Galvanostatic charge/discharge profile for the first, second, third cycles of N-RGO@MoS_2-10/S electrodes in the potential range of 1.5 V-3.0 V at 0.3C, (c) The cycle performance of cell for N-RGO/S and N-RGO@MoS_2-n/S electrodes at 0.3C, (d) The photograph of a polysulfide solution before and after exposure to the samples.

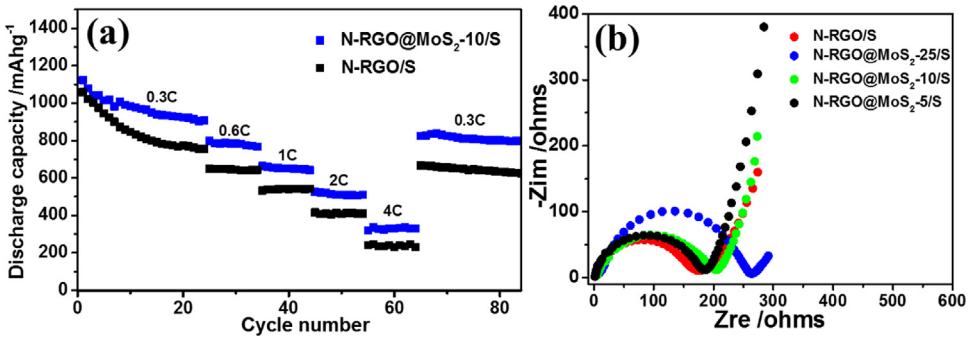

Fig. 6. (a) The rate capability of cell for N-RGO and N-RGO@MoS_2-10/S electrodes, (b) Electrochemical impedance spectra of N-RGO, N-RGO@MoS_2-25, N-RGO@MoS_2-10 and N-RGO@MoS_2-5.

decreases the conductivity of framework. Smaller amount of MoS_2 in N-RGO@MoS_2-5/S would weaken the interaction between MoS_2 and polysulfide, which leads to deteriorated durability of battery due to "shuttle effect". Fig. 5d shows the adsorption role of MoS_2 to polysulfide, we can find the different colour of the polysulfide solutions before and after exposure to the samples. The colour of the solution after adding N-RGO@MoS_2-10 is much lighter than that of N-RGO, which indicates the stronger absorption capability to polysulfide of N-RGO@MoS_2-10.

As shown in Fig. 6a, the rate capability of the N-RGO and N-RGO@MoS_2-10/S electrode is also investigated between 1.5-3.0 V. The discharge capacities of N-RGO@MoS_2-10/S electrode at 0.3C, 0.6C, 1C, and 2C after several cycles correspond to value of 907 mAh g^{-1}, 769 mAh g^{-1}, 642 mAh g^{-1} and 510 mAh g^{-1}, respectively. Even at a very high rate of 4C, the N-RGO@MoS_2/S-10 still presents a high specific capacity of 330.5 mAh g^{-1}. When the rate reduces back to 0.3C, a specific capacity of 824 mAh g^{-1} can still be restored, which indicates the excellent robustness and stability of N-RGO@MoS_2-10/S nanohybrids. In addition, the N-RGO@MoS_2-10/S electrode presents the better rate capability than the N-RGO/S electrode, which may be due to better dispersion of S after introduction of MoS_2. The remarkable rate capability of the N-RGO@MoS_2-10/S can be attributed to the fabrication of conductive network to shorten ion and charge diffusion distances, and the enhanced binding energy with sulfur to overcome shuttling effect.

In order to better understand the advanced performance of N-RGO@MoS_2-10, electrochemical impedance spectra (EIS) measurements are carried out. Electrochemical impedance spectras of the three electrodes show a semicircle in the high frequency and a linear region in the low frequency. The diameter of the semicircle is attributed to the charge transfer resistance associated with the electrochemical reaction at the electrode-electrolyte, and the inclined line refers to Warburg element related to the Li-ion diffusion in electrode. Fig. 6b shows the Nyquist plots of N-RGO@MoS_2-25/S, N-RGO@MoS_2-10/S, N-RGO@MoS_2-5/S and N-RGO/S electrodes at the open-circuit voltage before cycling. The impedances of N-RGO@MoS_2 gradually increase with the increasing of insulated MoS_2 in the nanohybrids, which suggests that moderate MoS_2 can slightly change the conductivity of nanohybrids, but excess MoS_2 is disadvantageous to the charges and ions transfer.

All in all, N-RGO@MoS_2 nanohybrids present great electrochemical properties as cathode of Li-S battery, which can be attributed to the following reasons. Firstly, the N-doping on RGO matrix by sulfourea introduces a great number of active nitrile groupings and fixes the defects on RGO, which leads to higher electrical conductivity and increases the compatibility between electrolyte and MoS_2. As followed, the improved compatibility reduces the size of MoS_2 NPs, which can be more uniformly dispersed on the doped RGO. Through facilitating the lithium ions and charges transfer of the structure, the charge/discharge capacity and rate performance are improved, simultaneously. In the last, MoS_2 NPs are composed of twist nanosheets, which supplies large surface area to absorb sulfur and the strong chemical interaction with polysulfide to relieve the shuttling effect. As the result, introduction of certain amount of MoS_2 on N-RGO can lead to the large capacity, excellent cycling stability and great rate performance.

4. Conclusions

In conclusion, the MoS_2 nanoclusters have been integrated with N-doped graphene oxide (N-RGO@MoS_2) by a facile hydrothermal method to successfully buildup conductive matrix for supporting sulfur. To explore the effect of MoS_2 in the nanohybrids, a series of samples with various content of MoS_2 are investigated to optimize the electrode performance. The experiment data reveals that the higher electronic conductivity of N-RGO can lead to great rate performance; the stronger interaction with polysulfide of MoS_2 can suppress the shuttle effect for an improved durability. As the result, N-RGO@MoS_2-10/S delivers an optimal discharge capacity of 729.1 mAh·g^{-1} at 0.3C with the coulombic efficiency of 97.3% after 180 cycles and 449.7 mAh g^{-1} at 0.5C after 600 cycles, which owns to improved balance between two components. This material will indicate a new route to rationally design cathode materials for Li-S batteries with superior stability and performance.

Acknowledgements

This work was supported by the National Natural Science Foundation of China (21572269, 21302224, and 21436003), and the Fundamental Research Funds for the Central Universities (17CX05015, 15CX08005A), The Key Research and Development Program of Shandong Province, China (2017GGX40118), Qingdao Science and Technology Plan (15-9-1-108-jch) and Graduate student innovation projects of China University of Petroleum (YCX2017038).

Appendix A. Supplementary data

Supplementary data associated with this article can be found, in the online version, at http://dx.doi.org/10.1016/j.electacta.2017.09.001.

References

[1] Y. Idota, T. Kubota, A. Matsufuji, Y. Maekawa, T. Miyasaka, Tin-Based Amorphous Oxide: A High-Capacity Lithium-Ion-Storage Material, Science 276 (1997) 1395–1397.
[2] Z. Li, G. Wu, S. Deng, S. Wang, Y. Wang, J. Zhou, S. Liu, W. Wu, M. Wu, Combination of uniform SnO_2 nanocrystals with nitrogen doped graphene for

high-performance lithium-ion batteries anode, Chem. Eng. J. 283 (2016) 1435–1442.
[3] J. Hu, Y. Jiang, S. Cui, Y. Duan, T. Liu, H. Guo, L. Lin, Y. Lin, J. Zheng, K. Amine, F. Pan, 3D-Printed Cathodes of $LiMn_{1-x}Fe_xPO_4$ Nanocrystals Achieve Both Ultrahigh Rate and High Capacity for Advanced Lithium-Ion Battery, Adv. Energy Mater. 6 (2016) 1600856.
[4] R.U.R. Sagar, N. Mahmood, F.J. Stadler, T. Anwar, S.T. Navale, K. Shehzad, B. Du, High Capacity Retention Anode Material for Lithium Ion Battery, Electrochim. Acta 211 (2016) 156–163.
[5] A. Manthiram, S.H. Chung, C. Zu, Lithium-sulfur batteries: progress and prospects, Adv. Mater. 27 (2015) 1980–2006.
[6] B. Zhang, X. Qin, G.R. Li, X.P. Gao, Enhancement of long stability of sulfur cathode by encapsulating sulfur into micropores of carbon spheres, Energy Environ. Sci. 3 (2010) 1531.
[7] P. Strubel, S. Thieme, T. Biemelt, A. Helmer, M. Oschatz, J. Brückner, H. Althues, S. Kaskel, ZnO Hard Templating for Synthesis of Hierarchical Porous Carbons with Tailored Porosity and High Performance in Lithium-Sulfur Battery, Adv. Funct. Mater. 25 (2015) 287–297.
[8] L. Ji, M. Rao, H. Zheng, L. Zhang, Y. Li, W. Duan, J. Guo, E.J. Cairns, Y. Zhang, Graphene oxide as a sulfur immobilizer in high performance lithium/sulfur cells, J. Am. Chem. Soc. 133 (2011) 18522–18525.
[9] C. Zu, A. Manthiram, Hydroxylated Graphene-Sulfur Nanocomposites for High-Rate Lithium-Sulfur Batteries, Adv. Energy Mater. 3 (2013) 1008–1012.
[10] H. Wu, Y. Huang, M. Zong, H. Fu, X. Sun, Self-assembled graphene/sulfur composite as high current discharge cathode for lithium-sulfur batteries, Electrochim. Acta 163 (2015) 24–31.
[11] Z. Ma, L. Tao, D. Liu, Z. Li, Y. Zhang, Z. Liu, H. Liu, R. Chen, J. Huo, S. Wang, Ultrafine nano-sulfur particles anchored on in situ exfoliated graphene for lithium–sulfur batteries, J. Mater. Chem. A 5 (2017) 9412–9417.
[12] J. Yan, B. Li, X. Liu, Nano-porous sulfur–polyaniline electrodes for lithium–sulfurbatteries, Nano Energy 18 (2015) 245–252.
[13] X. Liang, M. Zhang, M.R. Kaiser, X. Gao, K. Konstantinov, R. Tandiono, Z. Wang, H.K. Liu, S.X. Dou, J. Wang, Split-half-tubular polypyrrole@sulfur@polypyrrole composite with a novel three-layer-3D structure as cathode for lithium/sulfur batteries, Nano Energy 11 (2015) 587–599.
[14] F. Bottger-Hiller, P. Kempe, G. Cox, A. Panchenko, N. Janssen, A. Petzold, T. Thurn-Albrecht, L. Borchardt, M. Rose, S. Kaskel, C. Georgi, H. Lang, S. Spange, Twin polymerization at spherical hard templates: an approach to size-adjustable carbon hollow spheres with micro- or mesoporous shells, Angew. Chem. Int. Edit. 52 (2013) 6088–6091.
[15] S. Chen, X. Huang, H. Liu, B. Sun, W. Yeoh, K. Li, J. Zhang, G. Wang, 3D Hyperbranched Hollow Carbon Nanorod Architectures for High-Performance Lithium-Sulfur Batteries, Adv. Energy Mater. 4 (2014) 1301761.
[16] H.-J. Peng, T.-Z. Hou, Q. Zhang, J.-Q. Huang, X.-B. Cheng, M.-Q. Guo, Z. Yuan, L.-Y. He, F. Wei, Strongly Coupled Interfaces between a Heterogeneous Carbon Host and a Sulfur-Containing Guest for Highly Stable Lithium-Sulfur Batteries: Mechanistic Insight into Capacity Degradation, Adv. Mater. Interfaces 1 (2014) 1400227.
[17] Z. Xiao, Z. Yang, H. Nie, Y. Lu, K. Yang, S. Huang, Porous carbon nanotubes etched by water steam for high-rate large-capacity lithium–sulfur batteries, J. Mater. Chem. A 2 (2014) 8683.
[18] G. Zheng, Q. Zhang, J.J. Cha, Y. Yang, W. Li, Z.W. Seh, Y. Cui, Amphiphilic surface modification of hollow carbon nanofibers for improved cycle life of lithium sulfur batteries, Nano Lett. 13 (2013) 1265–1270.
[19] H.K. Jing, L.L. Kong, S. Liu, G. Li, X. Gao, Protected lithium anode with porous Al_2O_3 layer for lithium-sulfur battery, J. Mater. Chem. A 3 (2015) 12213–12219.
[20] S. Rehman, S. Guo, Y. Hou, Porous Carbon Spheres: Rational Design of Si/SiO_2 @Hierarchical Porous Carbon Spheres as Efficient Polysulfide Reservoirs for High-Performance Li-S Battery, Adv. Mater. 28 (2016) 3166.
[21] W.S. Zhi, W. Li, J.J. Cha, G. Zheng, Y. Yuan, M.T. Mcdowell, P.C. Hsu, C. Yi, Sulphur–TiO_2 yolk–shell nanoarchitecture with internal void space for long-cycle lithium–sulphur batteries, Nat. Commun. 4 (2013) 1331.
[22] Z. Li, J. Zhang, X. Lou, Hollow Carbon Nanofibers Filled with MnO_2 Nanosheets as Efficient Sulfur Hosts for Lithium-Sulfur Batteries, Angew. Chem. 54 (2015) 12886–12890.
[23] L. Hu, Y. Ren, H. Yang, Q. Xu, Fabrication of 3D hierarchical MoS_2/polyaniline and MoS_2/C architectures for lithium-ion battery applications, ACS Appl. Mater. Interfaces 6 (2014) 14644–14652.
[24] D. Chen, G. Ji, B. Ding, Y. Ma, B. Qu, W. Chen, J.Y. Lee, In situ nitrogenated graphene-few-layer WS_2 composites for fast and reversible Li^+ storage, Nanoscale 5 (2013) 7890.
[25] K. Chang, Z. Wang, G. Huang, H. Li, W. Chen, J.Y. Lee, Few-layer SnS_2/graphene hybrid with exceptional electrochemical performance as lithium-ion battery anode, J. Power Sources 201 (2012) 259–266.
[26] H. Wang, Q. Zhang, H. Yao, Z. Liang, H.W. Lee, P.C. Hsu, G. Zheng, Y. Cui, High electrochemical selectivity of edge versus terrace sites in two-dimensional layered MoS_2 materials, Nano Lett. 14 (2014) 7138–7144.
[27] Q. Zhang, Y. Wang, Z.W. Seh, Z. Fu, R. Zhang, Y. Cui, Understanding the Anchoring Effect of Two-Dimensional Layered Materials for Lithium-Sulfur Batteries, Nano Lett. 15 (2015) 3780–3786.
[28] D.-A. Zhang, Q. Wang, Q. Wang, J. Sun, L.-L. Xing, X.-Y. Xue, High capacity and cyclability of hierarchical MoS_2/SnO_2 nanocomposites as the cathode of lithium-sulfur battery, Electrochim. Acta 173 (2015) 476–482.
[29] W.S. Hummers Jr., R.E. Offeman, Preparation of graphitic oxide, J. Am. Chem. Soc. 80 (1958) 1339–1339.
[30] G. Yuan, G. Wang, H. Wang, J. Bai, Half-cell and full-cell investigations of 3D hierarchical MoS_2/graphene composite on anode performance in lithium-ion batteries, J. Alloys Compd. 660 (2016) 62–72.
[31] H. Tao, C. Yan, A.W. Robertson, Y. Gao, J. Ding, Y. Zhang, T. Ma, Z. Sun, N-Doping of graphene oxide at low temperature for the oxygen reduction reaction, Chem. Commun. 53 (2017) 873–876.
[32] C.-C. Wang, J.-W. Chang, S.-Y. Lu, p-Cu_2S/n-$Zn_xCd_{1-x}S$ nanocrystals dispersed in a 3D porous graphene nanostructure: an excellent photocatalyst for hydrogen generation through sunlight driven water splitting, Catal. Sci. Technol. 7 (2017) 1305–1314.
[33] Z. Li, L. Yuan, Z. Yi, Y. Liu, Y. Xin, Z. Zhang, Y. Huang, A dual coaxial nanocable sulfur composite for high-rate lithium-sulfur batteries, Nanoscale 6 (2014) 1653–1660.
[34] Z. Li, Y. Jiang, L. Yuan, Z. Yi, C. Wu, Y. Liu, P. Strasser, Y. Huang, A highly ordered meso@microporous carbon-supported sulfur@smaller sulfur core-shell structured cathode for Li-S batteries, Acs Nano 8 (2014) 9295.
[35] C. Zhang, H.B. Wu, C. Yuan, Z. Guo, X.W.D. Lou, Confining sulfur in double-shelled hollow carbon spheres for lithium-sulfur batteries, Angew. Chem. 124 (2012) 9730–9733.
[36] T. Lei, W. Chen, J. Huang, C. Yan, H. Sun, C. Wang, W. Zhang, Y. Li, J. Xiong, Multi-Functional Layered WS_2 Nanosheets for Enhancing the Performance of Lithium-Sulfur Batteries, Adv. Energy Mater. 7 (2017).
[37] X.Y. Yu, Y. Feng, Y. Jeon, B. Guan, X.W. Lou, U. Paik, Formation of Ni-Co-MoS_2 Nanoboxes with Enhanced Electrocatalytic Activity for Hydrogen Evolution, Adv. Mater. 28 (2016) 9006–9011.
[38] Y. Liu, L.-Z. Fan, L. Jiao, Graphene intercalated in graphene-like MoS_2: A promising cathode for rechargeable Mg batteries, J. Power Sources 340 (2017) 104–110.
[39] K. Hu, L. Tao, D. Liu, J. Huo, S. Wang, Sulfur-Doped Fe/N/C Nanosheets as Highly Efficient Electrocatalysts for Oxygen Reduction Reaction, ACS Appl. Mater. Interfaces 8 (2016) 19379–19385.
[40] Z. Wang, Y. Dong, H. Li, Z. Zhao, H.B. Wu, C. Hao, S. Liu, J. Qiu, X.W. Lou, Enhancing lithium-sulphur battery performance by strongly binding the discharge products on amino-functionalized reduced graphene oxide, Nat. Commun. 5 (2014) 5002.
[41] Y.X. Yin, S. Xin, Y.G. Guo, L.J. Wan, Lithium–sulfur batteries: electrochemistry, materials, and prospects, Angew. Chem. Int. Edit. 52 (2013) 13186–13200.
[42] J. Yoo, S.J. Cho, G.Y. Jung, S.H. Kim, K.H. Choi, J.H. Kim, C.K. Lee, S.K. Kwak, S.Y. Lee, COF-Net on CNT-Net as a Molecularly Designed, Hierarchical Porous Chemical Trap for Polysulfides in Lithium-Sulfur Batteries, Nano Lett. 16 (2016) 3292–3300.